Proceedings of the Thirty-sixth (2026) International Ocean and Polar Engineering Conference **www.isope.org**
Orlando, Florida, USA, May 31-June 5, 2026

ISBN 978-1-880653-72-2; ISSN 1098-6189

Design-Oriented Performance Assessment of a Gyroscopic Flywheel for Floating Offshore Wind Turbine Stabilization

Ping Cheng[1,2], Wenchuan Zhao[1], Tingyuan Zhang[1], Decheng Wan[2]*

[1] College of Logistics Engineering, Shanghai Maritime University, Shanghai, China
[2] Computational Marine Hydrodynamics Lab (CMHL), School of Ocean and Civil Engineering, Shanghai Jiao Tong University, Shanghai, China
*Corresponding author

ABSTRACT

In complex marine environments, the operational stability and safety of floating offshore wind turbines largely depend on the effective suppression of platform motion responses. This study conducts a design-oriented performance evaluation of the anti-roll gyro flywheel used to reduce platform pitch motion. Unlike comprehensive algorithmic optimization methods, the proposed approach focuses on improving the inertial distribution of the flywheel and assessing its roll-reduction effectiveness under actual sea conditions.

A three-dimensional coupled gyro-platform numerical model was established based on STAR-CCM+, employing unstructured meshes and boundary conditions that reflect actual marine environments. Both regular waves and irregular waves based on the JONSWAP spectrum are considered under different significant wave heights and wave periods. Key design parameters, such as flywheel mass distribution, are systematically investigated.

Numerical results indicate that the designed flywheel can generate effective gyroscopic control torque, demonstrating good pitch motion suppression for the platform. Compared to the baseline design, the optimized flywheel achieves a significant reduction in platform pitch response while maintaining a favorable balance between rotational inertia and structural mass. These results prove the engineering feasibility of the proposed anti-roll gyro flywheel design and provide practical reference for the application of gyro-stabilization systems in floating offshore wind platforms.

KEY WORDS: floating offshore wind turbine platform; gyroscopic stabilizer; flywheel design; motion suppression; numerical simulation

INTRODUCTION

Against the global imperative to address climate change, China has proposed the “dual-carbon” goals of achieving carbon peaking by 2030 and carbon neutrality by 2060 (Yang et al., 2022). As a clean and renewable energy technology, floating offshore wind power can optimize the energy structure and support the realization of these goals. Compared with conventional wind power systems, it can be deployed in deep and far-offshore waters, avoids occupying land resources, and makes better use of abundant and stable offshore wind energy, and is therefore regarded as an important direction for the future development of wind energy (Zheng et al., 2022). However, excessive motion response and insufficient stability of floating platforms remain major challenges in practical applications(Musial et al., 2023).

As an efficient motion control device, the gyrostabilizer has received increasing attention and has been applied in ship engineering, aerospace, and offshore floating structures(Zhilai et al., 2021). Depending on whether a precession control system is used, gyrostabilizers can be classified into active and passive types(LIU et al., 2022). Since the concept was first proposed by Schlick(1904), advancements in motor technology and materials have enabled modern gyrostabilizers to achieve lighter weight, more compact structure, and better stabilization performance, making them increasingly suitable for offshore engineering applications(Hong & Chen, 2012).

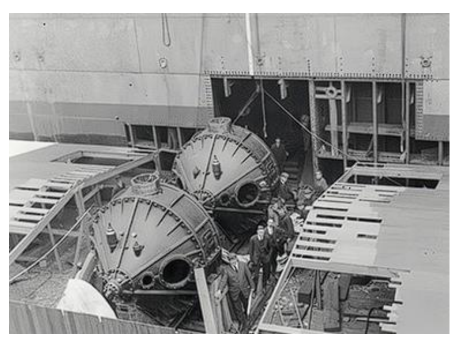

Fig.1. Dual Gyroscopic Roll Stabilizers on U.S. Military Transport Vessels

Gyrostabilizers were initially developed mainly for military applications. In 1912, after successful shore-based experimental verification, the first full-scale gyrostabilizer was installed on the aircraft carrier *Warden*(Hughes, 1971). Subsequently, multiple types of U.S. military transport vessels adopted this technology. By installing gyroscopic devices as illustrated in Fig.1, the roll motion amplitude of vessels was effectively controlled within 3°, even under severe wave conditions, thereby maintaining good stability(Baitis & Schmidt, 1989). With continuous technological advancements, the application of gyrostabilizers gradually expanded from military to civilian fields, particularly in yachts and luxury passenger ships(Rahiman et al., 2025). A representative example is the Italian luxury liner *Conte di Savoia*, constructed between 1932 and 1950 with a displacement of approximately 41,000 tons. Its gyroscopic stabilization system reduced roll amplitudes by about 60%, significantly enhancing navigation comfort and safety (Olaberria, 2018).

To improve the motion response of floating offshore wind turbine platforms under complex sea conditions, gyrostabilizer technology has been introduced as an effective stabilization measure. The gyroscopic moments generated by high-speed rotating flywheels can effectively suppress platform oscillations, particularly pitch motion, and thus enhance operational stability (Hu Y. et al., 2025; Sun et al., 2023). Nevertheless, conventional parameter design methods remain inadequate for balancing motion mitigation, power generation performance, and energy efficiency in complex marine environments (Liao et al., 2025). In this context, the flywheel rotor, as the core component of the gyrostabilizer, plays a decisive role in gyroscopic moment generation, dynamic coupling behavior, and system energy consumption(Hu L. et al., 2023). Hence, appropriate matching of rotor inertia, rotational speed, and mass distribution is crucial for achieving effective pitch suppression while avoiding excessive structural and energy penalties (Wu et al., 2021).

In summary, a properly designed flywheel rotor enhances gyroscopic moment output, improves pitch dynamic response, and reduces additional energy and structural burdens, serving as a key approach to improving pitch stability and overall system performance of floating offshore wind turbine platforms.

NUMERICAL METHOD

Dynamic model of the platform–gyroscope system

The OC4 (Offshore Code Comparison Collaboration Continuation) floating wind turbine platform project initiated by the International Energy Agency (IEA) selected the DeepCwind semi-submersible platform as the research object in Phase II. Owing to its typicality and representativeness, this platform has become a widely adopted benchmark model in the field of floating offshore wind turbine research. According to the standard floating wind turbine model defined by the IEA, the rotational motion equation of the platform can be simplified as follows (Jonkman, 2007):

$$I \cdot \ddot{\theta} + C \cdot \dot{\theta} + K \cdot \theta = \tau_{wave} + \tau_{wind} - \tau_{flywheel} \tag{1}$$

where I = rotational inertia of the platform, C = damping coefficient, K = restoring stiffness coefficient, $\ddot{\theta}$ = angular acceleration, $\dot{\theta}$ = angular velocity, and θ = angular displacement. τ_{wave} = wave-induced moment, τ_{wind} = wind-induced moment, and $\tau_{flywheel}$ = restoring moment provided by the gyroscopic flywheel.

To facilitate dynamic experiments on the floating wind turbine platform under laboratory conditions, the OC4 platform is scaled down according to the Froude similarity criterion. By maintaining the consistency of the ratio between gravitational force and inertial force, the platform is reduced at a scale of 1:50, enabling the scaled model to realistically reflect the motion characteristics of the prototype in dynamic tests. This approach not only avoids the difficulties associated with the excessive size of the prototype platform in terms of manufacturing and arrangement, but also significantly reduces experimental cost and safety risks. The main parameters of the scaled model are listed in Table 1, and its three-dimensional model is established using SolidWorks software, as shown in Fig. 2.

Table 1. Parameters of Different Simulation Conditions Basic parameters of the OC4 floating wind turbine platform and the corresponding scaled model parameters

Parameter	Full scale	Model scale
Mass / kg	$1.395\ 8\times10^{7}$	111.64
Maximum draft of platform / m	20	0.4
Diameter of upper column of side column / m	12	0.24
Diameter of base column of side column / m	24	0.48
Diameter of connecting members / m	1.6	0.032
Displacement / m^3	$1.391\ 7\times10^{4}$	0.1116
Distance from center of gravity to water surface / m	8.07	0.161
Roll moment of inertia / ($kg\cdot m^2$)	$1.397\ 4\times10^{10}$	44.63
Pitch moment of inertia / ($kg\cdot m^2$)	$1.555\ 2\times10^{10}$	49.76
Yaw moment of inertia / ($kg\cdot m^2$)	$1.369\ 2\times10^{10}$	43.81

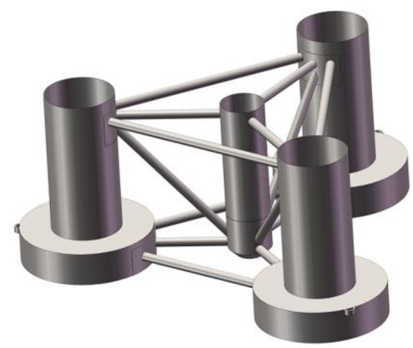

Fig.2. 3D model of a floating wind turbine platform

In the present study, the gyrostabilizer is assumed to be installed inside the platform near its center region and arranged symmetrically with respect to the platform centerline. This layout is adopted mainly to avoid additional mass eccentricity and undesired coupling effects caused by asymmetric installation. Under the rigid-body assumption used in this work, the gyroscopic stabilization effect is governed primarily by the angular momentum of the flywheel and its coupling with the platform pitching motion. Therefore, the installation location is not treated as a dominant design variable in the present analysis, provided that the gyroscope remains rigidly connected to the platform and does not introduce significant offset-induced inertia effects.

Basic principle of the gyroscopic stabilization system

The flywheel of the gyroscopic stabilizer is enclosed within a housing, and its spin axis is perpendicular to the precession axis. When the flywheel rotates at high speed, angular momentum is generated. The larger the angular momentum, the stronger the gyroscopic moment produced, and consequently, the more significant the motion suppression effect on the platform(Mashood & Singh, 2015). Therefore, angular momentum is a key indicator for evaluating the stabilization capability of a gyroscopic system, which can be expressed as:

$$L = I_z \omega \tag{2}$$

where L = angular momentum of the gyroscope, I_z = rotational inertia of the rotor about the spin axis, and ω = the rotational speed of the rotor. When the wind turbine platform is subjected to wave-induced pitching disturbance moments about the x-axis, the gyroscopic stabilization system rigidly connected to the platform responds synchronously. According to the principles of gyrodynamics, a high-speed rotating rotor subjected to an external moment will exhibit a precession motion perpendicular to the direction of the applied moment. The simplified structural model of the control moment gyroscope is illustrated in Fig. 3, which can be regarded as a combination of rigid-body planar motion and fixed-axis rotation.

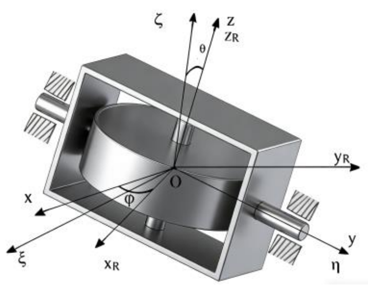

Fig.3. Simplified structural model of the anti-roll gyroscope

The base coordinate system $O-\xi\eta\zeta$ is fixed to the platform, while the gimbal coordinate system $O-xyz$ is used to describe the motion of the gyroscope. The X_R , Y_R ,and Z_R axes represent the longitudinal, transverse, and vertical directions of the outer frame, respectively, and are used to characterize the directional relationship between flywheel rotation and frame precession. θ denotes the precession angle, and φ represents the pitching angle. When the platform experiences pitching motion, causing the gyroscope housing to precess about the y-axis, the gyroscope generates a moment that is orthogonal to the precession plane. This gyroscopic moment is opposite in direction to the original pitching moment, thereby forming a restoring moment capable of suppressing the pitching motion. Consequently, the structural dimensions of the gyroscopic flywheel have a significant influence on the stabilization performance of the system.

Simulation Condition Setup

To simulate wave loads under realistic marine environments, this study employs the JONSWAP spectrum model to generate irregular waves(Fossen, 2011). This model effectively represents wave energy distribution, peak frequency, and spectral shape, and is commonly used to predict the dynamic response of floating structures under irregular wave action. Three typical operating conditions are selected for simulation analysis: Condition 1 is based on regular wave simulation, with wave height and period demonstrating the highest agreement with actual sea states; Condition 2 refers to related research by (Ma et al., 2018), where wave energy decay is minimal under these parameters, facilitating observation of system response; Condition 3 follows the reference sea state recommended by the international standard IEC 61400-3, ensuring the authority and generality of the experiments. Specific parameters for each condition are listed in Table 2.

Table 2. Parameters of Different Simulation Conditions

Condition No.	Wave Period (s)	Wave Height (m)
1	1.7	0.14
2	1.6	0.12
3	1.25	0.089

FLYWHEEL DESIGN SCHEME

Initial flywheel design scheme

Before conducting the structural optimization of the flywheel, an initial flywheel design scheme that satisfies the basic motion suppression requirements is first established as a reference baseline for subsequent optimization analysis. This initial scheme is not intended as a final engineering design, but rather as a reference configuration determined based on the fundamental working principles of the gyroscopic stabilizer and the dynamic requirements of the floating platform. Its primary purposes are twofold: (i) to verify the feasibility of the flywheel structure within the platform motion mitigation system, and (ii) to provide a unified performance benchmark for comparison with the optimized designs.

According to the pitching motion characteristics of the platform and the target stabilizing moment demand, the initial flywheel adopts a conventional solid disk configuration, with high-strength alloy steel selected as the material. The geometric dimensions and mass-related parameters of the flywheel are preliminarily estimated based on the angular momentum expression of the gyroscope, ensuring that sufficient angular momentum can be generated at the rated rotational speed to meet the stabilization requirements.

In addition, the flywheel size is determined according to the dynamic requirements of the 1:50 scaled platform model rather than by direct geometric scaling of a full-scale gyroscope. The design considers the stabilizing moment demand, the model-scale platform mass and displacement, the available installation space, and the allowable additional structural burden. Accordingly, the flywheel dimensions and mass are selected to provide sufficient angular momentum for pitch suppression while limiting their influence on the overall mass distribution and hydrostatic characteristics of the platform. For the present model, the initial flywheel mass is 4.5 kg, which remains small relative to the scaled platform mass of 111.64 kg.

The main parameters of the initial flywheel design include the flywheel radius, axial thickness, total mass, moment of inertia, and rated rotational speed. These parameters will be consistently compared with those of the optimized flywheel design in the subsequent comparative analysis.

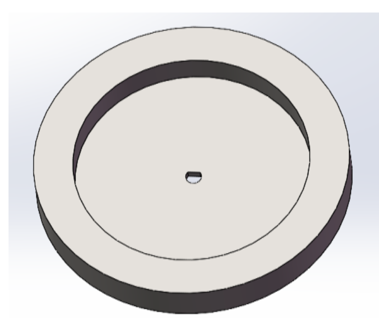

Fig.4. Flywheel rotor model before optimization

Optimization objectives and selection of design variables

To achieve the aforementioned optimization objectives, key structural parameters of the flywheel are selected as design variables, including the flywheel radius, axial thickness, and mass distribution pattern. These parameters directly influence the moment of inertia, structural stress level, and dynamic characteristics of the flywheel, and are therefore critical factors governing both stabilization performance and engineering cost.

During the optimization process, the following constraints are imposed:

(1) the equivalent stress of the flywheel at the maximum operating rotational speed must not exceed the allowable stress of the material;(2) no critical rotational speed or resonance risk is allowed to occur in the vicinity of the rated rotational speed;(3) the gyroscopic moment provided by the flywheel under the target sea state must satisfy the platform pitching suppression requirement.
By introducing these constraints, non-engineering optimization results caused by an excessive pursuit of stabilization performance can be effectively avoided.

Optimized flywheel design scheme

As shown in Figure 5, the overall structural design philosophy of the optimized flywheel centers on the core principle of "lightweight design and inertia concentration." This is achieved by combining a thickened outer rim with a hollowed inner core to strike a rational balance between rotational inertia and structural mass. Specifically, concentrating the primary mass at the outer rim of the flywheel allows for a significant increase in the moment of inertia under the same mass condition, thereby yielding greater angular momentum output. This enhances the torque output efficiency of the roll stabilization gyro. Concurrently, the extensive hollowing of the central portion of the flywheel effectively removes inner-ring material that contributes minimally to inertia. This substantially reduces the flywheel's total mass and motor drive power consumption, improving the system's energy efficiency ratio(Dongxu et al., 2023).

Fig.5. Optimized flywheel rotor model

To balance structural strength with manufacturing feasibility, the flywheel adopts a tri-symmetric support arm connection structure. This configuration ensures overall symmetry in mass distribution while effectively distributing centrifugal forces generated under high-speed rotation, mitigating local stress concentrations, and maintaining excellent dynamic balancing performance(Zhang et al., 2025). Compared to solid disc or multi-arm designs, the three-arm structure offers lower structural redundancy and manufacturing costs while meeting strength requirements. Furthermore, an arc transition design is employed between the support arms and the rim to avoid stress concentrations caused by sharp geometric features. This promotes a more uniform stress distribution under high-speed rotation, thereby enhancing the flywheel's fatigue resistance and long-term operational reliability.
A standard shaft hole structure is incorporated at the flywheel's center to facilitate assembly with the drive shaft, ensuring load transfer symmetry, and making it suitable for the high-speed operating conditions of the roll stabilization gyro system. Additionally, the exterior design utilizes smooth surfaces and continuous transitions. This not only helps improve aerodynamic or fluid dynamic resistance characteristics during rotation, reducing additional disturbances, but also enhances cooling conditions and operational stability. The overall symmetrical and uniform mass distribution further minimizes eccentric forces and imbalance responses, providing robust support for the flywheel's stable operation in complex marine environments. The numerical results of the flywheel optimization are presented in Table 3.

Table 3. Comparison table of optimization results

Optimization Parameter	Pre-optimization Flywheel Rotor	Post-optimization Flywheel Rotor
Mass (kg)	4.5	
Density (kg/m³)	7850	
Radius (m)	0.10	0.12
Thickness (m)	0.018	0.021
Moment of Inertia I_{yy} (kg·m²)	0.027	0.031
Moment of Inertia I_{xx} (kg·m²)	0.014	0.015
Moment of Inertia I_{zz} (kg·m²)	0.014	0.015

STRUCTURAL AND DYNAMIC VALIDATION OF THE FLYWHEEL

Static and Structural Strength Validation

To ensure the engineering feasibility of the optimized flywheel structure, static strength analysis is first conducted. The flywheel material selected is cast alloy steel, with a yield strength of 241.3 MPa. The rotational stress state of the flywheel at 3000 rpm is calculated using the finite element method.
The analysis shows that under the rotational load at 3000 rpm, the maximum von Mises stress in the flywheel is 26.97 MPa, accounting for only 11.17% of the material's yield strength, indicating ample safety margin. When the rotational speed is increased to 5000 rpm, the maximum stress rises to 85.31 MPa, which is still only 35.39% of the yield strength, demonstrating that the structure possesses a high reserve of static strength within the target operating speed range.

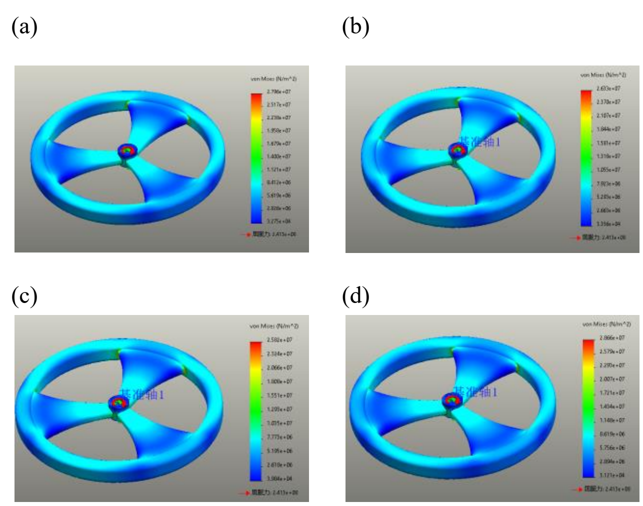

Fig.6. Grid convergence analysis

To verify the mesh independence of the finite element calculation results, a systematic mesh convergence analysis is conducted in this study. As shown in Figure 6, four grid element size division schemes are sequentially adopted: (a) 9 mm, (b) 6 mm, (c) 3 mm, and (d) local refinement in stress concentration areas with 1.5 mm. Comparing the maximum equivalent stress values under the target conditions for each scheme reveals that the calculation results gradually stabilize as the mesh is refined. Notably, the stress variation from scheme (c) to the locally refined mesh (d) is less than 3%, which meets the widely accepted 5% convergence criterion in engineering analysis. This confirms the reliability of the numerical solution and provides a credible basis for subsequent strength assessment and optimization design.

Fatigue Strength Analysis

To ensure the operational safety of the flywheel under long-term high-speed rotation conditions, this section evaluates the high-cycle fatigue strength of its critical areas based on the stress-life method. Since the flywheel primarily experiences cyclic centrifugal stress, its potential failure mode is high-cycle fatigue, making fatigue assessment more critical than static strength verification.

Analysis Method and Key Parameters

A stress-based fatigue analysis method was employed, utilizing the Goodman criterion to account for the effects of mean stress. The criterion formula is as follows:

$$\frac{\sigma_a}{S_e} + \frac{\sigma_m}{S_{ut}} = \frac{1}{n_f} \tag{3}$$

where σ_a = stress amplitude, σ_m = mean stress, S_e = modified fatigue limit of the material, S_{ut} = ultimate tensile strength of the material, and n_f = fatigue safety factor.

The determination of key correction factors is as follows: Stress concentration factor K_f : Stress concentration in the flywheel primarily occurs at the transition fillet connecting the rim and the support arms. After local mesh refinement in this region, the peak stress σ_{max} = 58.3 MPa and nominal stress σ_{nom} = 28.4 MPa were extracted, yielding a theoretical stress concentration factor $K_t = \sigma_{max} / \sigma_{nom} \approx 2.05$. Considering the notch sensitivity of cast alloy steel, the notch sensitivity factor was taken as $q = 0.8$, and the fatigue strength reduction factor was calculated:

$$K_f = 1 + q(K_t - 1) = 1.84 \tag{4}$$

Fatigue limit modification: The basic fatigue limit of the material S_e was taken as $0.5 \times S_{ut}$. Considering actual engineering conditions, the surface finish factor k_a=0.8 , the size factor k_b=0.9 , and the reliability factor k_c=0.897 were introduced. Thus, the modified fatigue limit of the component under actual service conditions is:

$$S_e = \frac{S_e' \times k_a \times k_b \times k_c}{K_f} \approx 42.5\,\text{Mpa} \tag{5}$$

Load Spectrum and Fatigue Assessment

The most severe condition of 5000 rpm was selected as the baseline for assessment. Finite element analysis shows that under this condition, the maximum alternating stress amplitude in the flywheel is $\sigma_a = 42.66$ MPa, and the mean stress is $\sigma_m = 42.66$ MPa. Substituting the data into the Goodman criterion, The calculated sum of equivalent stresses is 1.180, corresponding to a fatigue safety factor of $n_f = 1/1.180 \approx 0.85$. The initial calculation indicates an insufficient safety factor.

Design Improvement and Final Validation

As shown in Figure 7, based on the above results, the transition fillet was locally optimized geometrically, reducing the stress concentration factor K_t to 1.6. After recalculation, the fatigue strength reduction factor K_f was updated to 1.48, and the corrected fatigue limit S_e increased to 52.1 MPa. The Goodman criterion was reapplied for evaluation, yielding a combined equivalent stress of 0.996 and a fatigue safety factor $n_f \approx 1.004 > 1$, which meets the engineering requirements.

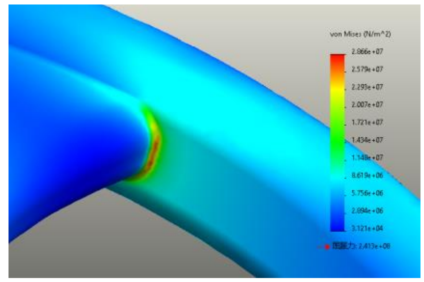

Fig.7. Local stress diagram of the flywheel

In summary, after local structural optimization, the fatigue strength at the critical locations of the flywheel satisfies the requirements for long-term operation at and below the rated speed of 5000 rpm, thereby preventing high-cycle fatigue failure.

DYNAMIC CHARACTERISTICS AND CRITICAL SPEED ANALYSIS

Overview of the Analysis Method

To assess the dynamic stability of the flywheel rotor under high-speed operating conditions and prevent resonance, this section establishes an analysis model based on rotor dynamics theory and defines the criteria for determining critical speeds.

(1) The flywheel and its supporting shaft system of the anti-roll gyro are modeled as a rotating elastic body with distributed mass and stiffness characteristics. Its dynamic equation under rotation can be expressed as:

$$[\mathrm{M}]\{\ddot{\mathrm{u}}\} + [\mathrm{C}]\{\dot{\mathrm{u}}\} + \Omega[\mathrm{G}]\{\dot{\mathrm{u}}\} + [\mathrm{K}]\{\mathrm{u}\} = \{\mathrm{F}\} \tag{6}$$

where: $[\mathrm{M}]$ is the mass matrix, $[\mathrm{C}]$ is the structural damping matrix, $[\mathrm{G}]$ is the gyroscopic matrix, $[\mathrm{K}]$ is the equivalent stiffness matrix including centrifugal stiffening effects, Ω is the angular velocity of the flywheel, $\{\mathrm{u}\}$ is the generalized displacement vector, $\{\mathrm{F}\}$ is the external excitation force vector.

This equation comprehensively considers inertia, damping, gyroscopic effects, and stiffness changes induced by rotation, making it suitable for describing the dynamic behavior of the flywheel rotor during operation.

(2)Natural Frequency Solution and Speed-Sweeping Modal Analysis：

To investigate how the system's natural frequencies vary with rotational speed, damping $[\mathrm{C}]$ and external excitation $\{\mathrm{F}\}$ are neglected, and harmonic motion is assumed ($u = \phi e^{i\omega t}$). Substituting into Equation (6) yields the eigenvalue problem:

$$(K - \omega^2 M + i\Omega\omega G)\phi = 0 \tag{7}$$

Solving this eigenvalue problem provides the complex eigenvalues of the system at different rotational speeds Ω . The imaginary parts correspond to the system's natural frequencies ω. Due to the presence of the gyroscopic matrix G, the frequencies of forward and backward precession modes split as the rotational speed changes—a manifestation of the gyroscopic effect.

To fully capture this characteristic, this study employs speed-sweeping modal analysis. Within the range from 0 to twice the rated speed, the rotational speed Ω is varied incrementally. The eigenvalue problem is solved at each step to extract the first few natural frequencies $\omega(\Omega)$, thereby obtaining a complete dataset describing the frequency-speed dependency.

(3) Critical Speed Determination Criterion：For rotating machinery, one of the most common excitation sources is mass unbalance of the rotor itself, whose excitation frequency is synchronized with the rotational frequency—this is the 1× rotational frequency excitation. The relationship between the excitation frequency f_n and the rotational angular velocity Ω is:

$$f_n = \frac{\omega_n}{2\pi} \tag{8}$$

Plotting f_n against the corresponding rotational speed Ω yields a straight line through the origin, termed the 1× excitation line. Superimposing the modal frequency curves $\omega(\Omega)$ obtained from the speed-sweeping analysis onto the same plot creates a Campbell diagram. The critical speed is defined as the rotational speed at which a modal frequency curve intersects the 1× excitation line. If the operating speed falls near a critical speed, resonance occurs, leading to a sharp increase in dynamic response amplitude and potential structural failure. Therefore, by examining whether the frequency curves intersect the excitation line in the Campbell diagram, one can visually assess whether resonance risk exists across the entire operating speed range, thereby validating the rationality of the flywheel's dynamic design.

Results and Discussion

As shown in the figure 8, based on the results of the speed-sweeping modal analysis, the Campbell diagram for the flywheel structure is plotted. The horizontal axis represents the flywheel speed, the vertical axis represents frequency, solid lines of different colors indicate the variation curves of the first four natural frequencies of the flywheel under rotating conditions, the thick dashed line represents the 1× excitation line, and the thin dashed line represents the 2× excitation line.

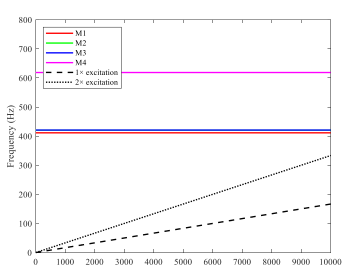

Fig.8. Campbell diagram of the flywheel structure

From the Campbell diagram, it can be observed that within the 0–10000 rpm speed range, the first four natural frequencies of the flywheel exhibit stable evolution trends with increasing speed. No intersections occur between these frequency curves and the 1× or 2× excitation lines near the rated operating speed. This indicates that the designed flywheel possesses good dynamic stability under high-speed rotation, with effective isolation between its structural modes and rotational excitation, ensuring no resonance occurs during normal operation.

Combined with the preceding static strength and fatigue analysis results, it can be concluded that the flywheel meets the engineering application requirements in terms of both structural safety and dynamic rationality. This provides a reliable guarantee for its long-term stable operation within the anti-roll gyro system and on the floating wind turbine platform.

PERFORMANCE COMPARISON OF ROLL REDUCTION UNDER DIFFERENT OPERATING CONDITIONS

Simulation Condition Setup and Results

To visually compare the suppression effects of different flywheel designs on platform pitch motion, the study utilized Star-CCM+ software to conduct numerical simulations under the three conditions proposed in Table 1 for the three configurations: "gyro off," "pre-optimized flywheel," and "post-optimized flywheel." Figure 9 presents the time-history curves of the platform pitch angle under each condition. (a) (b) (c) correspond to condition 1, 2 and 3 respectively.

(a)

(b)

(c)

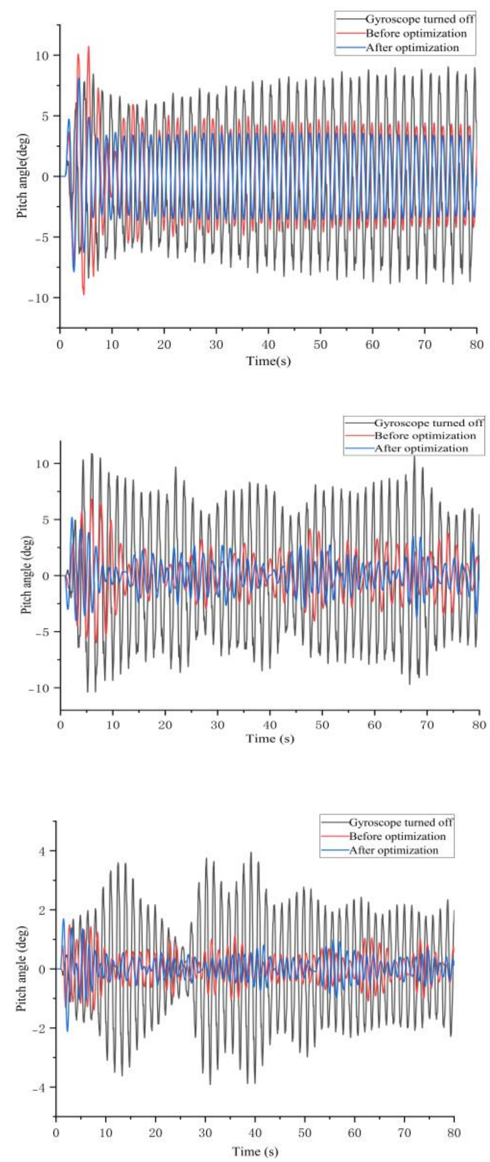

Fig.9. Comparison diagrams of three operating conditions under different configurations

From Figure 9(a) (Condition 1), it can be observed that the oscillation amplitude is largest with the gyro off, averaging around ±7.5°. The pitch amplitude of the post-optimization flywheel (±3°) is significantly lower than that of the pre-optimization flywheel (±5°). Moreover, the post-optimization flywheel not only reduces the amplitude but also results in smoother motion, indicating a more rational inertial distribution that can more effectively resist large-amplitude disturbances.

From Figure 9(b) (Condition 2), it can be seen that the overall motion amplitude is smaller than in Condition 1. The curves for the pre- and post-optimization flywheels are close in certain time segments, but the peaks of the post-optimization flywheel are clearly lower. The gyro-off configuration still exhibits the largest amplitude. Under moderate sea states, the absolute reduction in motion achieved by optimization may be less pronounced than under severe conditions, but the peak suppression effect remains significant. This demonstrates that the optimized design performs stably across various sea states.

From Figure 9(c) (Condition 3), the overall motion amplitude is the smallest, and all three curves are relatively smooth. However, the amplitude of the post-optimization flywheel remains noticeably lower than that of the pre-optimization flywheel, particularly in the 60–80 second interval. The gyro-off configuration still shows relatively the largest fluctuations. This indicates that even under relatively calm sea conditions, flywheel optimization can further suppress minor oscillations, enhancing platform stability.

From the pitch angle time-history curves, it can be concluded that under all three irregular wave conditions and across varying sea states, the optimized flywheel structure significantly reduces the platform pitch response. Furthermore, as the sea state worsens, the performance improvement brought by optimization becomes more pronounced. This demonstrates that the optimized flywheel rotor can effectively suppress platform pitch motion under random wave excitation. However, due to the randomness in phase and amplitude of the irregular waves generated by the spectrum-based model in STAR-CCM+, relying solely on peak values or local features of the time-domain curves makes it difficult to accurately and objectively quantify the roll reduction effects under different flywheel design conditions. Therefore, it is necessary to introduce the Root Mean Square (RMS) value to comprehensively evaluate the platform pitch response, providing a more thorough and reliable reflection of the performance improvement achieved through flywheel structural optimization.

Comparison of Platform Pitch Response

To quantitatively assess the improvement effect of flywheel structural optimization on the pitch motion of the semi-submersible floating wind turbine platform, a comparative analysis of the platform pitch response before and after optimization was conducted under identical irregular wave conditions and identical gyro rotational speeds. The steady-state time segment from 30 s to 80 s was selected, and the root mean square (RMS) value of the platform pitch angle was calculated as the evaluation index. The calculation result is shown in Figure 10.

The platform pitch reduction rate is defined as the relative reduction in the RMS of the pitch angle before and after optimization. Its expression is as follows:

$$\eta = \frac{RMS_{baseline} - RMS_{optimized}}{RMS_{baseline}} \times 100\% \quad (9)$$

Under Condition 1 (wave period 1.7 s, wave height 0.14 m), the RMS of the platform pitch angle was 3.03° when using the pre-optimized flywheel structure and decreased to 2.47° when using the post-optimized structure. The corresponding pitch amplitude reduction rates were 45% and 55%, respectively. The results indicate that flywheel structural optimization can effectively reduce the platform pitch response level without changing the rotational speed.

Under Condition 2 (wave period 1.6 s, wave height 0.12 m), the RMS values of the platform pitch angle before and after optimization were 1.86° and 1.46°, respectively, corresponding to reduction rates of 63% and 71%. Compared to Condition 1, despite changes in wave excitation parameters, the flywheel structural optimization still demonstrates a stable roll reduction effect, indicating that this optimization scheme possesses good adaptability and robustness to different irregular wave conditions.

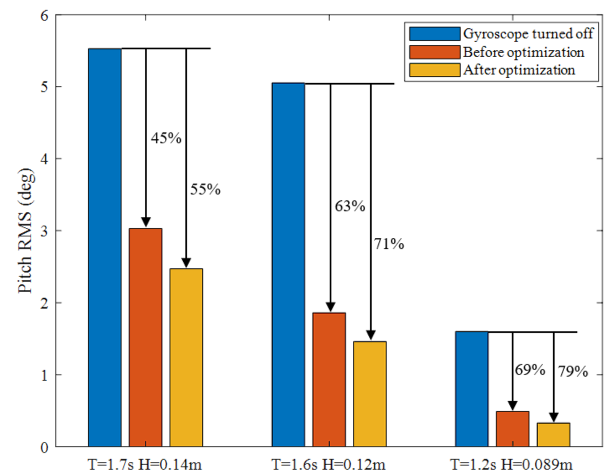

Fig.10. RMS value of platform pitch angle under different working conditions

Under Condition 3 (wave period 1.2 s, wave height 0.089 m), the RMS of the platform pitch angle decreased from 0.49° before optimization to 0.33° after optimization, corresponding to a reduction rate of 79%. This result further shows that even under relatively calm sea conditions, the optimized flywheel structure can still effectively suppress platform pitch motion, demonstrating its applicability across a wide range of sea states.

Integrating the comparative results from the three sets of irregular wave conditions reveals that under all sea states, the optimized flywheel structure significantly reduces the RMS value of the platform pitch response, with reduction rates ranging between 55% and 79%. Since the compared configurations differ only in flywheel structure (pre- vs. post-optimization), without introducing additional drive or control parameter adjustments, the aforementioned performance improvement is entirely attributable to the optimized inertial distribution achieved through flywheel design.

This result demonstrates that reasonable improvement of the flywheel structure alone can significantly enhance the pitch motion suppression capability of the anti-roll gyro on the floating wind turbine platform, without increasing system energy consumption, mass, or control complexity. This structural optimization approach provides an effective technical pathway characterized by lightweight design and low additional burden for improving the motion stability of floating wind power platforms under random waves.

CONCLUSIONS

This study focuses on the design and performance evaluation of a flywheel rotor for the anti-roll gyroscope system used in floating wind turbine platforms. The primary objective is to enhance the platform's pitch motion stability through structural optimization of the flywheel, without increasing system complexity or energy consumption.

A design-oriented evaluation methodology is proposed, emphasizing the improvement of the flywheel's inertial distribution. A three-dimensional coupled gyro-platform numerical model is established using STAR-CCM+ software, considering both regular and JONSWAP-spectrum-based irregular waves under varying significant wave heights and periods. The key design parameters, particularly the flywheel's mass distribution, are systematically investigated.

An optimized flywheel structure is developed based on the principle of "lightweight design and inertia concentration," achieved by combining a thickened outer rim with a hollowed inner core and employing a tri-symmetric support arm configuration. Comprehensive validation analyses are conducted, including static strength assessment, fatigue life evaluation based on the Goodman criterion, and dynamic stability analysis via critical speed determination using Campbell diagrams. The results confirm that the optimized flywheel possesses sufficient structural strength, adequate fatigue resistance, and excellent dynamic stability within the target operational speed range, meeting the requirements for long-term service in marine environments.

Numerical simulations under three typical sea conditions demonstrate that the optimized flywheel structure significantly reduces the platform's pitch motion. Quantitative analysis based on the Root Mean Square (RMS) of the pitch angle shows that the optimized design achieved pitch reduction rates between 55% and 79% across different sea states, compared to the baseline (pre-optimization) design. This performance improvement is attributed solely to the optimized inertial distribution, as no additional control parameters or rotational speed adjustments are introduced.

In summary, the proposed flywheel design and optimization approach effectively enhances the pitch motion suppression capability of the anti-roll gyroscope system for floating wind turbine platforms. It offers a feasible, lightweight technical pathway to improve platform stability in random wave environments, contributing to the operational safety and efficiency of floating offshore wind energy systems. Future work may explore multi-objective optimization considering broader operational conditions and integrated platform-gyroscope control strategies.

It should be noted that the wave conditions considered in this study correspond to the model scale and are primarily intended for mechanism investigation and comparative evaluation of gyrostabilizer performance. Although the present results provide useful insight into the influence of flywheel design on platform pitch suppression, direct extrapolation to full-scale offshore engineering applications still requires further validation under realistic sea states and scale-consistent similarity analysis.

ACKNOWLEDGEMENTS

This work is supported by the National Natural Science Foundation of China (52301328), to which the authors are most grateful.

REFERENCES

Baitis, A. E., & Schmidt, L. V. (1989). "Ship Roll Stabilization in the U.S. Navy," *Naval Engineers Journal*, *101*(3), 43–53.

Dongxu, H., Xingjian, D., Wen, L., Yangli, Z., Xuehui, Z., Haisheng, C., & Zhilai, Z. (2023). "A review of flywheel energy storage rotor materials and structures," *Journal of Energy Storage*, *74*, 109076.

Fossen, T. I. (2011). Handbook of marine craft hydrodynamics and motion control. *John Willy & Sons Ltd*.

Hong, C., & Chen, Y.-X. (2012). "Current situation and tendency of development of ship stabilizer technique, "*Ship Engineering*, *34*(S2), 236–244.

Hu, L., Zhang, M., Yu, X., Yuan, Z.-M., & Li, W. (2023). Real-time control of ship's roll motion with gyrostabilisers. *Ocean Engineering*, *285*, 115348.

Hu, Y., Ji, H., Liu, J., Huang, C., Huang, Z., Zhang, Y., Lei, J., Chen, W., Dong, Q., & Chen, C. (2025). "Comparative analysis of dynamic and structural responses of three floating offshore wind turbine foundations," *Ocean Engineering*, *320*, 120252.

Hughes, T. P. (1971). *Elmer sperry*. Johns Hopkins University Press.

Jonkman, J. M. (2007). *Dynamics modeling and loads analysis of an offshore floating wind turbine*. University of Colorado at Boulder.

Liao, L., Huang, Q., Wang, L., Yang, J., Song, D., Chen, S., & Huang, L. (2025). "Data-Driven Load Suppression and Platform Motion Optimization for Semi-Submersible Wind Turbines," *Journal of Marine Science and Engineering*, *13*(10), 1839.

LIU, Y., XIA, Z., TANG, Y., ZHANG, J., & FAN, S. (2022). "On Ship Roll Stabilization Based on Gyrostabilizer," *Ship & Boat*, *33*(04), 124.

Ma, S., Ge, W., Ertekin, R. C., He, Q., & Duan, W. (2018). "Experimental and Numerical Investigations of Ship Parametric Rolling in Regular Head Waves," *China Ocean Engineering*, *32*(4), 431–442.

Mashood, K. K., & Singh, V. A. (2015). "Rotational kinematics of a rigid body about a fixed axis: Development and analysis of an inventory," *European Journal of Physics*, *36*(4), 045020.

Musial, W., Spitsen, P., Duffy, P., Beiter, P., Shields, M., Mulas Hernando, D., Hammond, R., Marquis, M., King, J., & Sathish, S. (2023). *Offshore Wind Market Report: 2023 Edition* (No. NREL/TP-5000-87232). Washington, D.C.: U.S. Department of Energy (DOE).

Olaberria, J.-P. (2018). *Ship design-knowledge in early modern Europe: Royal yachts and the shared knowledge of ship-designers and common shipwrights*[PhD Thesis, University of Southampton].

Rahiman, W., Ghazali, M. H. M., & Mahmood, I. A.-T. (2025). "Revolutionizing Marine Stability: A Review of Cutting-Edge Gyro Stabilizer Designs and Techniques for Vessels," *IEEE Access*.

Schlick, E. (1904). "The gyroscopic effect of flywheels on board ship," *Transactions of the Institute of Naval Architects*, *23*(1), 117–134.

Sun, J., Cai, Z., Sun, J., & Jin, D. (2023). "Dynamic analysis of a rigid-flexible inflatable space structure coupled with control moment gyroscopes," *Nonlinear Dynamics*, *111*(9), 8061–8081.

Wu, X., Chen, Y., & Liu, Y. (2021). "Structure optimization of metal rotor of grid-connected flywheel energy storage system," *Acta Energ. Solaris Sinica*, *42*, 317.

Yang, P., Peng, S., Benani, N., Dong, L., Li, X., Liu, R., & Mao, G. (2022). "An integrated evaluation on China's provincial carbon peak and carbon neutrality," *Journal of Cleaner Production*, *377*, 134497.

Zhang, H., Teng, W., Qin, R., Wang, Y., & Liu, Y. (2025). "Stability analysis of composite energy storage flywheel rotor," *Journal of Mechanical Science and Technology*, *39*(3), 1073–1087.

Zheng, L. I., Xiaojiang, G. U. O., Xuhui, S., & Haiyan, T. (2022). "Summary of technologies for the development of offshore wind power industry in China," *Power Generation Technology*, *43*(2), 186.

Zhilai, H., Xinyuan, L., & Dongping, J. (2021). "Output characteristic analysis of single gimbal control moment gyroscope," *Chinese Journal of Theoretical and Applied Mechanics*, *53*(2), 511–523.